



Computational alloy design, synthesis, and characterization of WMoNbVCr_x refractory high entropy alloy prepared by vacuum arc melting

Ammar Basil Nader Alkraidi ^{a,b,*}, Mubashir Mansoor ^{b,c}, Burçak Boztemur ^{a,b}, Hasan Gökçe ^{a,d}, Faruk Kaya ^{b,e}, Cennet Yıldırım ^{b,f}, Bora Derin ^b, Duygu Ağaoğulları ^{a,b}, M. Lütfi Öveçoğlu ^{a,b,g,*}

^a Istanbul Technical University, Department of Metallurgical and Materials Engineering, Particulate Materials Laboratories (PML), Graphene & 2D Materials Laboratory, Maslak, Istanbul 34469, Türkiye

^b Istanbul Technical University, Department of Metallurgical and Materials Engineering, Maslak, Istanbul 34469, Türkiye

^c Istanbul Technical University, Department of Applied Physics, Maslak, Istanbul 34469, Türkiye

^d Istanbul Technical University, Prof. Dr. Adnan Tekin Materials Science and Production Technologies Applied Research Center (ATARC), Maslak, Istanbul 34469, Türkiye

^e Hittit University, Department of Metallurgical and Materials Engineering, Corum 19030, Türkiye

^f TENMAK Boron Research Institute, Ankara, Türkiye

^g MEF University, Dept. of Mechanical Engineering, Ayazağa, Saryer, Istanbul 34396, Türkiye



ARTICLE INFO

Keywords:

Refractory high entropy alloy

Alloy design

Arc melting

Wear resistance

Microhardness

ABSTRACT

Prior investigations have demonstrated enhanced mechanical properties, such as hardness and wear resistance, through high-entropy alloy designs that contain refractory metals. We propose the WMoNbVCr_x alloy phase space as a single-phase BCC-structured, hard, and refractory high-entropy alloy for the first time. The WMoNbVCr_x alloy ($x = 0, 0.25, 0.5, 0.75$, and 1) system is investigated computationally through CALPHAD and DFT for the equimolar and non-equimolar compositional phase spaces and synthesized through vacuum arc melting. The DFT calculations demonstrated the excellence of specific non-equimolar compositional spaces. It was found that stoichiometries rich in W and poor in V are exceptionally hard, while those rich in V and poor in W demonstrate unprecedented toughness, as determined by the ductility descriptor (Pugh's Ratio). The computational analysis shows the significance of microstructures that contain both (W-rich and W-poor) solid solution, where a synergy between hardness and toughness is created. Our experimental synthesis using vacuum arc melting demonstrated the possibility of successfully producing these alloys with W-rich (dendritic) and W-poor (interdendritic) solid solution regions, starting from elemental powders. The introduction of chromium (Cr) resulted in enhanced microhardness and wear resistance. The peak microhardness was attained when 0.5 moles of Cr were added, reaching 7.03 ± 0.24 GPa, accompanied by the least wear volume loss. The produced alloys were found to align with the computationally predicted-designed alloys in terms of the hardness and Young's modulus trends that they follow. This comprehensive investigation underscores the synergistic application of CALPHAD and DFT techniques in the tailored design of novel high-entropy alloys, explaining their synthesis, structural correspondence, and the pivotal role of Cr in enhancing the mechanical properties of these alloys.

1. Introduction

Due to their exceptional features, high entropy alloys (HEAs) have attracted researchers worldwide to investigate this material group thoroughly and study their potential properties. In 2004, Yeh et al. proposed alloys with at least five major elements, each being 5–35 at% can potentially exhibit unique properties [1–4]. Refractory high entropy

alloys (RHEAs), which are a subset of HEAs, were introduced by Senkov et al. in 2010 by producing WN₆MoTa and WN₆VMoTa alloys [5]. RHEAs exhibit outstanding hardness [6,7] and wear resistance [8–10], which make them potential candidates for extreme environment applications [11]. Until April 2021, 3541 HEAs publications have been reported [12], which reflects the global interest in these new families of alloys and their vast compositional potential. However, even with this

* Corresponding authors at: Istanbul Technical University, Department of Metallurgical and Materials Engineering, Particulate Materials Laboratories (PML), Graphene & 2D Materials Laboratory, Maslak, Istanbul 34469, Türkiye.

E-mail addresses: alkraidi17@itu.edu.tr (A.B.N. Alkraidi), ovecoglu@itu.edu.tr (M. Lütfi Öveçoğlu).

immense global effort in researching high entropy materials, the vastness of the high entropy phase space and its combinatorial possibilities puts forth a great challenge on the allocation of time and resources towards finding the useful compositions.

The enormous possibilities for developing these new alloys require tools and methodologies beyond conventional experimental trial and error. Computational simulation of materials' properties can potentially help accelerate the production and investigation of these alloys to predict their possible combinations and investigate their properties efficiently. [3,13,14]. In other words, the experimental route towards exploring this vast compositional phase space is rather restrictive. The main challenge in high entropy materials is that even if a given combination of elements does give rise to a single-phase structure, the addition of each element and the molar stoichiometry can drastically influence the macroscopic properties, including mechanical moduli, which makes the experimental journey extremely difficult. Therefore, computational modeling from an atomistic perspective makes targeted experimental design possible, thus accelerating the process of novel material discovery [15]. Amongst the most used computational tools, Calculation of Phase Diagrams (CALPHAD) and Density Functional Theory (DFT) stand out for their success in collating with experimental data [16,17]. To name a few noteworthy studies, Gao et al. reported 16 RHEAs, compared the theoretically predicted to the previously used empirical parameters, and found that CALPHAD is more efficacious [18]. Shaikh et al. [19] studied 126 quaternary and 126 quinary equiatomic RHEAs. They used CALPHAD to predict the number of phases at a specific temperature, which proved extremely helpful due to insufficient data on the thermodynamic stability of high entropy alloys. In a recent study [20], 1451 alloys were investigated to identify single-phase non-equiatomic HEA using the CALPHAD approach, and elastic constants, along with their thermal properties, were determined using DFT. The predicted alloys were later prepared using vacuum arc melting to validate the predictions, which proved highly effective.

The general trend in synthesizing high entropy materials is based on producing equimolar compounds, where the stoichiometric contribution of each alloying element is equal. This is found in the thermodynamic tendency for systems to explore states of maximum disorder. Therefore, equimolar compositions are advantageous to maximize the configurational entropy, driven by the statistical likelihood of adopting a vast array of configurations. This is in accord with the second law of thermodynamics, which asserts that systems tend to evolve towards states with higher entropy. Thus, the HEA phase evolution at higher temperatures is more likely due to the dominance of the entropic contribution in Gibbs free energy. The underlying concept in this regard was beautifully demonstrated and explained by the idea of Entropy Forming Ability (EFA), as introduced in the study by Sarker et al. [21] which aligns with the statistical nature of entropy. By employing DFT for computational analysis, the study delves into the statistical distribution of formation energies for various atomic configurations within a solid solution. As a measure of the spread in the energy landscape, the standard deviation of these energies reflects the statistical variance and, by extension, the configurational entropy of the system. A similar concept is well demonstrated by Henrick et al. [22] as well. Although, from the perspective of increasing configurational entropy, the equimolar stoichiometry of alloying elements is favored, there is a rising trend in high entropy research that demonstrates non-equimolar configurations can potentially outperform their equimolar counterparts for an array of different functionalities, including corrosion resistance [23] and mechanical properties such as hardness and wear resistance [10].

Regarding synthesizing novel RHEAs, vacuum arc melting is one of the most commonly used approaches for consolidating RHEA due to their high melting temperatures [24]. However, vacuum arc melting leads to macro and micro elemental segregation, mainly in the form of fine dendritic structures accompanying RHEA prepared by melting from the liquid state. This segregation affects the alloys' wear and hardness properties because the elemental distribution would lead to variation in

local hardness, thus affecting the wear properties accordingly. However, the robustness of this synthesis technique has made it an attractive alternative to powder-metallurgy-based production techniques, such as spark plasma sintering (SPS), hot press (HP), hot isostatic press (HIP), etc., that tend to produce homogenous microstructures.

A key focal point of research in the RHEAs is on enhancing the mechanical properties of such alloys for improved hardness and wear resistance. An upcoming trend in the literature is addition of certain alloying elements that are significantly smaller in their atomic radii to promote solid solution strengthening induced by lattice distortion. For example, Fang et al. [25] have found that introducing Cr into $ZrNbTaHf_{0.2}Cr_x$ promotes creating a laves phase in the interdendritic region, which led to an improvement in hardness from 352.9 Hv to 530 Hv after adding 1 mol of Cr. Similarly, in the $WMoNbTiCr_x$ alloy, microstructure refinement, solid solution strengthening, and laves phase strengthening contributed to the hardness increase up to 9.73 GPa after adding 20 at% of Cr [26], which suggests Cr addition can be a powerful strategy for enhancing hardness in RHEAs. Similarly, it was found that the yield strength of $AlCr_xNbTiV$ improved with the increase in Cr content due to laves phase precipitation and solid solution strengthening induced by lattice distortion that resulted from introducing smaller atomic radius Cr atoms [27,28].

RHEAs typically exhibit high hardness, and many of these alloys contain elements that form stable oxide layers that protect the underlying material from further wear and degradation, which makes them good candidates for wear resistance applications. Yet the efficacy of RHEAs under abrasive wear conditions necessitates a thorough investigation. On one hand, in the realm of RHEAs, few alloys have investigated the tribological properties [29–33], some have studied the effect of Al addition on these alloys [34], and some have induced the formation of oxide layers to improve the tribological properties [35]. On the other hand, Cr addition has been shown to improve the wear properties of conventional alloys [36–39] but few have investigated the effect of Cr addition in HEAs on wear properties [40,41].

The aim of our study is to investigate W, Mo, Nb, and V combinatorial phase space as the base alloying elements because they belong to the refractory group of elements and have a BCC crystal structure, which can avoid intermetallic phase formation [36–41]. We studied the impact of variations in compositional stoichiometry and how the local changes in composition (micro-segregation) during arc-melting affect the mechanical properties. We also study the impact of Cr addition and its induced effects on the alloy to further elucidate the reasoning behind the effectiveness of Cr addition for improved mechanical properties. We produced a new family of RHEAs based on CALPHAD and DFT modeling and compared the results with experimentally synthesized alloys produced by vacuum arc melting. We demonstrate the significance of the non-equimolar phase space and the importance of deviating from the equimolar structures through a synergetic comparison of results from quantum chemical theoretical studies by DFT and experimental characterizations.

2. Computational and experimental methods

2.1. Computational methods

The elements were selected based on the Hume-Rothery rules of solid solution formation. Prior studies have investigated refractory alloys of $WMoNbTaCr$, $WMoNbTa$, and $WMoNbHf$ systems, to name a few [5,42]. However, the introduction of Cr and V to $WMoNb$ has not been published. Therefore, the baseline alloy $WMoNbV$ is selected for this investigation, which is unique, and Cr was added in 0.25 mol increments to synthesize $WMoNbVCr_x$ high entropy alloys ($x = 0, 0.25, 0.5, 0.75$, and 1). All the constituent elements have the BCC Bravais lattice with close atomic radii, which significantly enhances the entropy-forming ability of this alloy system. Table 1 lists the properties of the alloy's constituents. Phase diagrams and alloy systems that might yield desired

Table 1
Properties of the elements used to produce the alloys.

Element	Atomic Radius (Å)	Melting Point °C	Electronegativity
W	2.02	3422	2.36
Mo	2.01	2623	2.16
Nb	2.08	2477	1.6
V	1.92	1890	1.63
Cr	1.85	1857	1.66

microstructures have already been identified using thermodynamic models that employ the Calculated Phase Diagram (CALPHAD) technique in the research of HEAs [3].

Thermochemical simulations were performed using the Calculated Phase Diagram module (CALPHAD) of FactSage 8 to predict the possible phases in these RHEAs. FStel database was chosen for the possible solid and liquid solution phase formations. The CALPHAD approach has already been extensively used in the exploration of HEAs to model phase diagrams and to identify, predict, and quantify the chemical composition of the alloy, proving to be an indispensable tool for the discovery of novel materials, as mentioned before in the introduction section. Spin-polarized density functional theory (SP-DFT) has been used to calculate the lattice parameters, hardness, thermodynamic functions, and elastic properties of alloys with various chemical compositions. To better understand the impact of different solid solution compositions on the mechanical properties, we generated $3 \times 3 \times 3$ SQS-type supercells of body-centered cubic (BCC) structure, corresponding to a periodic cell of 54 atoms. The sites have been populated with W, V, Nb, Mo, and Cr in equimolar and various non-equimolar percentages (based on experimentally obtained XRD and point EDS data of the synthesized samples). The generalized gradient approximation was used, as parametrized by Perdew Burke and Ernzerhof (GGA-PBE) [43]. Planewave cut-off energy of 500 eV was applied, and the Gaussian integration scheme was utilized with a smearing of 0.05 eV. The self-consistent field (SCF) convergence criterion of 10^{-6} eV was used for all calculations with a blocked Davidson algorithm. The cell parameters and atomic coordinates could relax until Hellmann-Feynman forces are below a threshold value lower than 10 meV/Å. A k-point spacing of 0.25 \AA^{-1} was utilized during SCF calculations, which corresponds to a $3 \times 3 \times 3$ k-mesh grid, forced to be centered at Γ . The reciprocal space and projector augmented wave method (PAW) [44] were used for all of the DFT calculations, as implemented in the Vienna ab initio simulation package (VASP 6.1) under the framework of MedeA 3.4. The elastic constants were then calculated by creating strained cells (0.05 strain on each strained supercell in various orientations) to solve for the elastic constants [45,46] using Eq. 1.

$$\frac{E_{\text{tot}}^{\text{strained}} - E_{\text{tot}}^{\text{relaxed}}}{V_0} = \frac{1}{2} \sum_{i=1}^6 \sum_{j=1}^6 C_{ij} e_i e_j \quad (1)$$

Here, $E_{\text{tot}}^{\text{strained}}$ and $E_{\text{tot}}^{\text{relaxed}}$ are the total energy of a strained and unstrained supercell, respectively, and V_0 is the initial volume of the cell. The atoms of the strained supercells were relaxed until Hellmann-Feynman forces fell to a value lower than 10 meV/Å. Twelve distinct strained supercells were used for total energy calculations, which were then used to deduce the elastic constant C_{ij} and the associated engineering strains e as shown in Eq. 1. Twelve structures been used, due to C1 symmetry considerations and allowing maximum degrees of freedom for the atomic displacements. The elastic moduli including bulk (B), shear (G), Young's (Y), along with the Poisson's ratio were then calculated through the principles of elasticity as proposed by the Voigt and Hill models [47], as given below.

$$G = \frac{1}{2} \left(\frac{C_{11} - C_{12} + 3C_{44}}{5} + \frac{5}{4(S_{11} - S_{12}) + 3S_{44}} \right) \quad (2)$$

$$B = \frac{2G}{3} \left(\frac{1 + \sigma}{1 - 4\sigma} \right) \quad (3)$$

$$Y = \frac{9B}{1 + \frac{3B}{G}} \quad (4)$$

To estimate the alloy ductility, we have employed the methodology described in detail by Senkov and Miracle [48] for calculating the Pugh's ratio (B/G ratio). The fracture toughness (K_{IC}) is also calculated using Eq. 5, based on a prior study on BCC materials [49], where V_a is the volume of the supercell per atom. The Eq. 5 is based on the theoretical findings of Niu et al. [54], where elastic moduli are correlated to fracture toughness values. We have omitted the $1 + \alpha$ prefactor given the similarity of the alloy compositions and the fact that we intend to find a relative comparison between the alloys and their base alloy counterparts. The $K_{\text{IC}}^{\text{REF}}$ is taken as the equimolar base value and the comparative results are given in the supplementary file.

$$K_{\text{IC}} = \left(G \left(\frac{G}{B} \right)^{\frac{1}{2}} V_a^{\frac{1}{6}} \right) / K_{\text{IC}}^{\text{REF}} \quad (5)$$

The Vickers hardness (H_v) values were calculated using the model proposed by Tian et al. [50]. The thermal expansion coefficient and the thermodynamic functions were calculated through the Grüneisen-Debye approximation [51], which are provided as supplementary data. This methodology has been proven to be successful in the calculation of mechanical properties for high entropy materials, as shown in recent studies [52–54].

2.2. Experimental methods

The elemental powders were blended using Turbula 3-dimensional mixer for 2 hours. The composition of each blend is listed in Table 2. The mixed powders were pressed under a uniaxial pressure of 370 MPa ($370 \times 10^6 \text{ N/m}^2$) in a MSE MP-0710 hydraulic press (cold pressed-CP). The cylindrical green compacts weighed around 6 g each and were then consolidated inside water-cooled copper crucibles using a compact arc melter (MAM-1 by Edmund Buehler). The melting chamber was vacuumed and purged with high-purity argon 4 times before each melting session. Each sample was remelted 4 times and flipped after each melt to ensure a homogenous microstructure. It was kept in a liquid state for up to 1 minute upon each melt. The produced ingots were button-shaped with lustrous surfaces, indicating no oxidation occurred during melting.

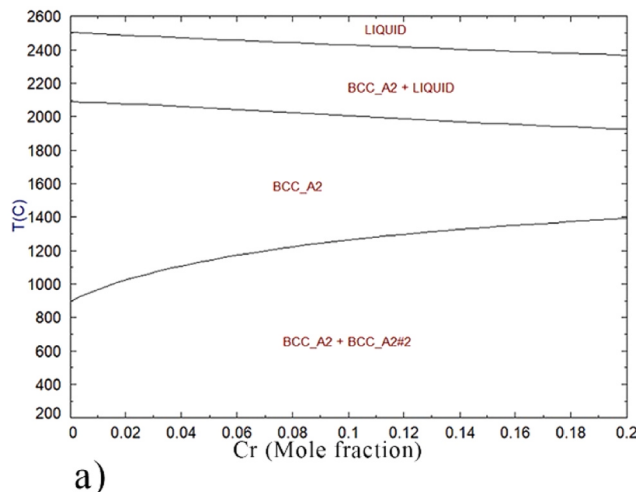
The density of the alloys (as cast) was measured with an AccuPyc pycnometer. The pycnometer cell volume was 10 cm^3 , and the volume of the samples was determined with an accuracy of $\pm 0.0001 \text{ cm}^3$ by measuring the free volume of the loaded cell using He gas for ten purge cycles. X-ray diffraction (XRD) investigations were performed using a Bruker™ D8 Advanced Series X-ray powder diffractometer with $\text{CuK}\alpha$ ($\lambda = 0.154 \text{ nm}$, 35 kV, and 40 mA) radiation in the 2θ range of $20\text{--}90^\circ$ with a step size of 0.02° at a rate of $2^\circ/\text{min}$. The peaks were indexed using

Table 2
Chemical composition of the prepared blends (atm./wt%).

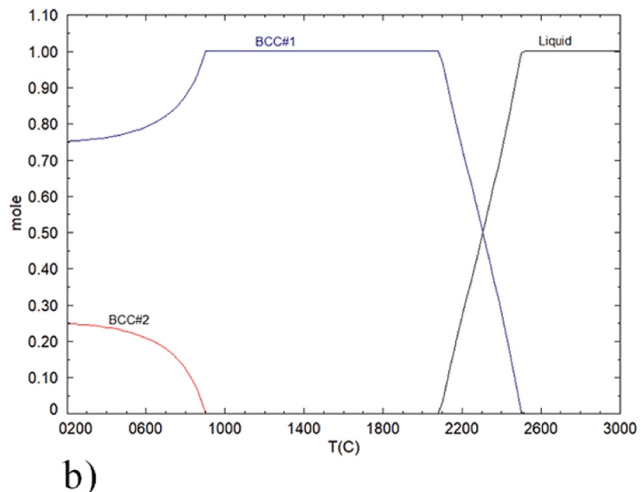
Sample Name	Abbr.	W	Nb	Mo	V	Cr
WNbMoV	Cr0	25/ 43.39	25/ 21.93	25/ 22.65	25/ 12.02	0
WNbMoVCr _{0.25}	Cr0.25	23.53/ 42.1	23.53/ 21.28	23.53/ 21.98	23.53/ 11.67	5.88/ 2.29
WNbMoVCr _{0.5}	Cr0.5	22.22/ 40.89	22.22/ 20.66	22.22/ 21.34	22.22/ 11.33	11.11/ 5.78
WNbMoVCr _{0.75}	Cr0.75	21.05/ 39.74	21.05/ 20.08	21.05/ 20.74	21.05/ 11.01	15.79/ 8.43
WNbMoCr	Cr1	20/ 38.65	20/ 19.53	20/ 20.17	20/ 10.71	20/ 10.93

powder diffraction files (ICDD). JEOL NeoScope JCM6000 SEM was used for morphology and composition analysis using a field emission scanning electron microscope with an energy-dispersive X-ray spectrometer (EDS). The cross-sectioned ingot surfaces in as-cast condition were prepared for microhardness measurements using a Vickers hardness tester (Shimadzu HM-124; Akashi, Japan) under a load of 4.98 N with a loading time of 20 s, and an average of 20 indentations has been

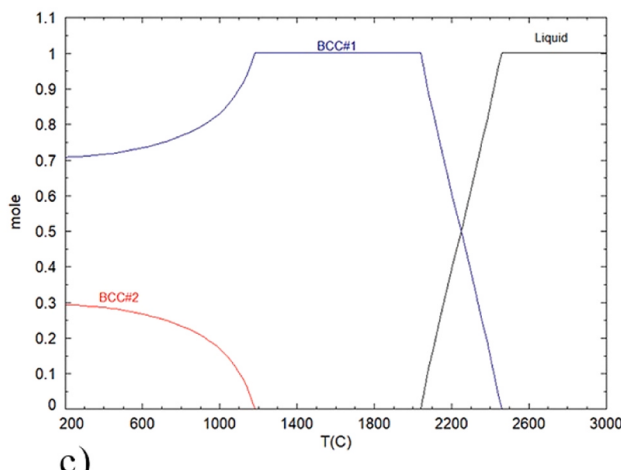
reported. Moreover, the samples were subjected to reciprocating linear wear tests on a polished surface using a Tribotechnic-type TRIBOTester against a 6 mm-diameter Al₂O₃ ball as a counterface. Wear testing conditions were selected as a sliding speed of 6 mm/s, a sliding distance of 50 m, and a wear track length of 2 mm. The tests were performed with a normal load of 5 N at room temperature. Also, wear track 2-D profiles were screened by a surface profilometer (Veeco Dektak 6 M) to measure



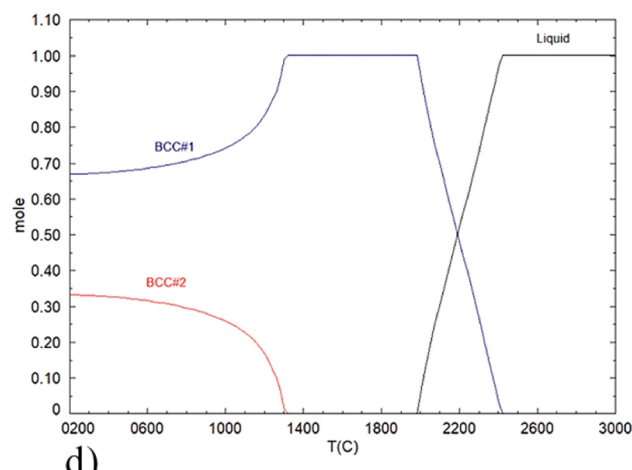
a)



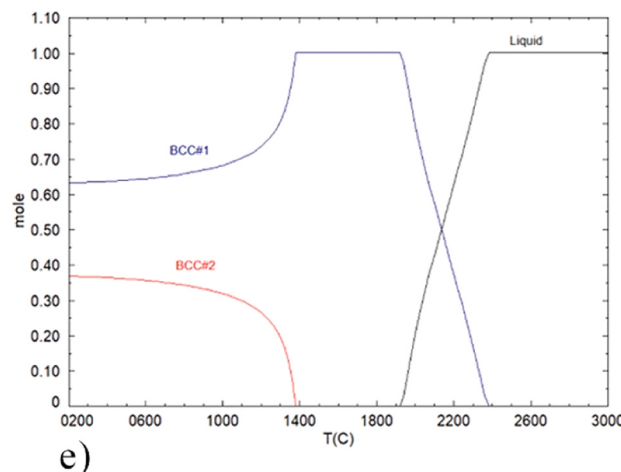
b)



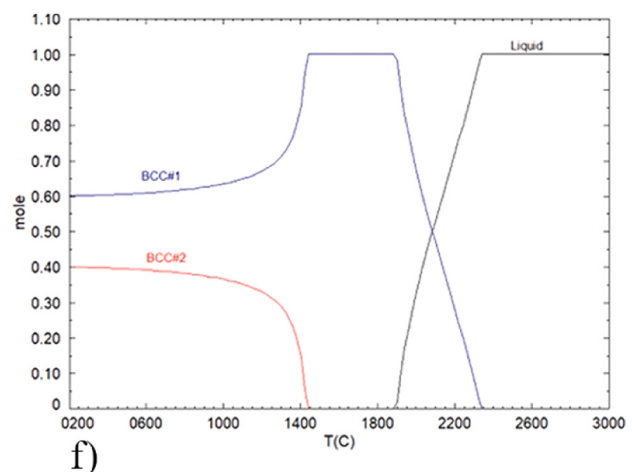
c)



d)



e)



f)

Fig. 1. FactSage 8 (a) calculated WMoNbVCr_x equilibrium phase diagram and mole fraction versus temperature where in (b) x=0, (c) x=0.25, (d) x=0.5, (e) x=0.75 and (f) x=1 mol.

the wear volume loss. X-ray photoelectron spectroscopy (XPS) analysis was performed on deposited films on RHEAs using a Thermo Scientific/K-Alpha Brand XPS Device with monochrome Al $\text{K}\alpha$. All tests were carried out at a 400 μm spot size. Nano-indentation tests were carried out using Anton Paar NH3 with linear loading at room temperature, an applied load of 100 mN and loading-unloading rate of 200 mN/min with a dwindle time of 10 seconds using Berkovich diamond indenter and Oliver & Pharr method. X-ray photoelectron spectroscopy (XPS) analysis was performed on deposited films on RHEAs using a Thermo Scientific/K-Alpha Brand XPS Device with monochrome Al $\text{K}\alpha$. All tests were carried out at a 400 μm spot size. Nano-indentation tests were carried out using Anton Paar NH3 with linear loading at room temperature, an applied load of 100 mN, and a loading-unloading rate of 200 mN/min with a dwindle time of 10 seconds using the Berkovich diamond indenter and the Oliver & Pharr method.

3. Results and discussion

3.1. Computational-aided alloy design

Thermochemical simulation results through CALPHAD are illustrated in Fig. 1. The models predict the formation of BCC#1 phase below the melting temperature for all of the alloy systems, starting from the base alloy with 0 Cr (i.e., WMoNbV) up to 1 mol (i.e., WMoNbVCr) in equimolar composition. Also, it predicts that BCC#1 is formed for a wide range of temperatures, followed by BCC#2 at low temperatures only, which may occur during the cooldown. Depending on the molar percentage of Cr, the simulation predicts the formation of BCC#2 phase when the temperature drops below 1400 °C in the case of the highest Cr content (i.e., the equimolar WMoNbVCr alloy), and reducing the Cr content reduces the formation temperature of BCC#2 down to 900 °C in the base alloy. As the content of Cr increases, the alloy's melting temperature decreases as well, while increasing the formation temperature of BCC#2.

Fig. 1(a) shows the predicted phase diagram generated by FactSage, while Fig. 1(b-f) are isopleth diagrams that are often used to interpret the impact of compositional variations on the phase equilibria over a wide range of temperatures to compare the phase formation during cooling or heating over a series of compositions. As the temperature goes below 2500 °C, a single BCC structure starts to form, and a single-phase region is seen down to 900 °C, as shown in 1-b, while after adding 1 mol of Cr, the BCC2 starts to form at temperatures below 1400 °C as seen in Fig. 1(f). For the WMoNbV alloy in Fig. 1(b), it is predicted that at 600 °C the alloy would consist of 79.2 % BCC#1, which is rich in higher melting temperature elements that are W, Mo, Nb and poor in V and 20.08 % BCC#2, which is V rich. As the content of Cr increases, Fig. 1(c) to (f), BCC#2 becomes rich in low melting temperature elements that are V and Cr and poor with other constituents. BCC#2 phase reaches 39.13 % in the highest Cr content alloy, WMoNbVCr.

DFT modeling, when using the nominal composition atomic percentages, predicts that adding Cr increases the hardness of the alloy, primarily due to solid solution strengthening, while a consistent decrease in density and lattice parameter is inevitable as smaller and lower density Cr is introduced to the base alloy. The maximum hardness value calculated by DFT for the nominal compositions is 4.95 GPa, as

seen in Table 3.

However, considering the BCC#1 and BCC#2 outputs from CALPHAD, DFT calculations have been carried out on two such cases that are given in Table 4. It was found that the non-equimolar case with a W-rich composition can have a hardness of over 10 GPa, whereas the V-rich case is seen to have a significantly low hardness of less than 2 GPa. The calculated thermal expansion coefficients and heat capacity values are also shown in Fig. 2. This extreme variation in the hardness based on variations in stoichiometry of the same phase space demonstrates the significance of the non-equimolar stoichiometric compositions for creating highly tailored properties.

In summary, based on the computational results, a single phase BCC structured WMoNbVCr_x high entropy alloy was predicted that can be synthesized experimentally, and two main solid solution stoichiometries of the same phase should emerge (BCC#1:W-rich and BCC#2:V-rich). The calculated mechanical properties show the excellence of non-equimolar stoichiometries, as an increase in W can lead to a doubling of the hardness values. Therefore, the formation of a solid solution with a microstructure that is locally W-rich (hard and relatively brittle) and V-rich (soft and relatively more ductile) is predicted, which can further enhance this alloy's wear properties, as seen from the elastic properties that are provided in detail under the supplementary files and the following sections.

3.2. Microstructural and characterization results of the synthesized RHEA

XRD patterns of the WMoNbVCr_x as cast ingots are presented in Fig. 3 (a). A single BCC phase and a minor Laves phase are shown at the diffraction peaks. Fig. 3(b) of an enlarged portion of the XRD pattern at 40.6° 2θ shows a consistent peak shift to a higher 2θ value, which indicates a decrease in the lattice parameter. This decrease in lattice constant is due to a smaller atomic radius of Cr being introduced to the matrix that hosts elements of relatively larger atomic radii. The XRD peaks of the synthesized alloys are close to the d-spacings of pure W and Mo, and the peaks indicate the formation of a single-phase BCC that is consistent with the CALPHAD modeling results as well. The minor peak closely matches the Laves phase C15 that typically accompanies Cr containing RHEAs, as mentioned before in the literature [25,41,55].

The intensity of the Laves phase indicates a low volume fraction of this phase. As the content of Cr exceeds 0.25 moles, the peak intensity increases, which implies an increase in the volume fraction of this phase. Fig. 4 shows SEM images of the cross-section of the WMoNbVCr ingot. Due to different cooling rates that take place during solidification from the molten state, a fine dendritic structure was observed on the edge of the sample that is close to the surface in contact with the argon atmosphere and the bottom surface that was in contact with the water-cooled copper crucible. Meanwhile, larger equiaxed grains at the center region of the sample were observed, where a slower cooling rate is expected.

As the amount of Cr being introduced to the base alloy (WMoNbV) increased, thicker and more defined interdendrites were discernible since Cr mainly segregates into this region, and the difference is more apparent when comparing the base alloy SEM image and equimolar WMoNbVCr alloy in Fig. 5(a) and (e), respectively.

The produced ingots had various compositional stoichiometries due to the solidification sequence and the segregation accompanying

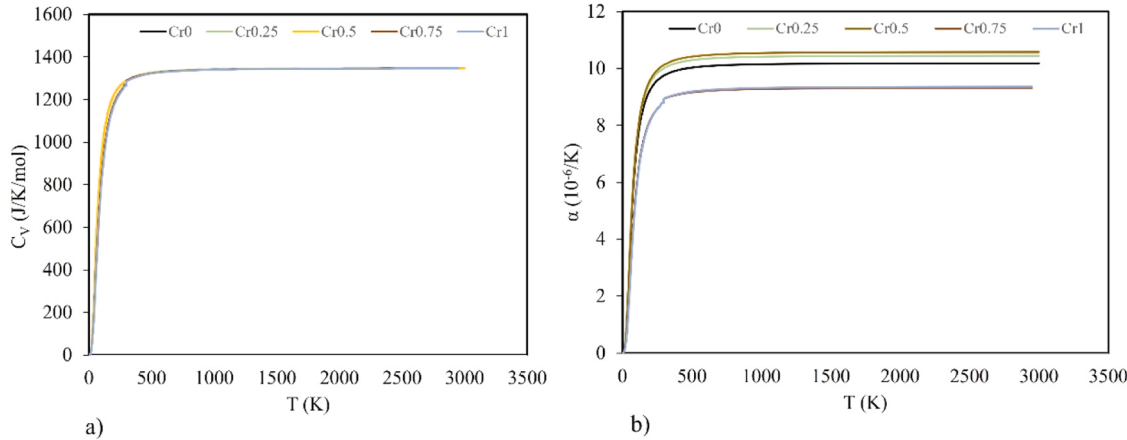
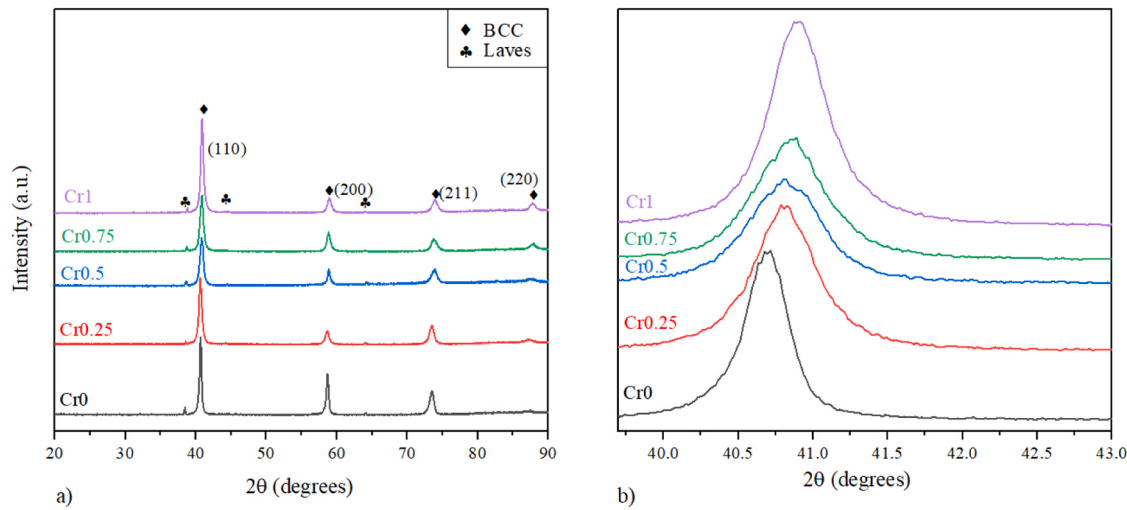
Table 3
DFT calculated Vicker's microhardness, lattice parameters, and density of designed alloys.

Alloy	W	Mo	Nb	V	Cr	Hv (GPa)	a (Å)	ρ (g/cm ³)
WMoNbV	25 %	25 %	25 %	25 %	0 %	3.24	3.161	11.071
WMoNbVCr _{0.25}	23.53 %	23.53 %	23.53 %	23.53 %	5.88 %	3.07	3.140	11.021
WMoNbVCr _{0.5}	22.22 %	22.22 %	22.22 %	22.22 %	11.11 %	3.09	3.128	10.806
WMoNbVCr _{0.75}	0.2105	0.2105	0.2105	0.2105	0.1579	4.68	3.114	10.785
WMoNbVCr	20 %	20 %	20 %	20 %	20 %	4.95	3.102	10.367

Table 4

DFT calculations show the compositional effect on alloy properties.

Solid solution type	Atomic %					Hv (GPa)	ρ (g/cm ³)	a (Å)
	W	Mo	Nb	V	Cr			
W-rich	44.2	24.2	15.8	12	3.8	10.18	13.37	3.167695
V-rich	6.6	13.9	27.6	31.4	20.5	1.66	8.796	3.095294

**Fig. 2.** (a) Variations of vibrational heat capacity C_v (b) Variations of thermal coefficient of linear expansion (α) with temperature.**Fig. 3.** a) XRD patterns of arc melted WMoNbVCr_x alloys and b) zoomed in view on main BCC phase showing a consistent peak shift to larger Bragg angles with increasing Cr content.

solidification. Segregation takes place as a result of different melting temperatures of the constituents to form dendritic and interdendritic structures with variation in the composition of each, proving to be W-rich dendrites and V-rich interdendrites, as predicted by CALPHAD calculations and as seen in the mapping analysis in Fig. 6. From the mapping images, it can be seen in Fig. 6(a) and (b) that W and Mo are localized mainly in the dendritic region, though Mo is more evenly distributed to the interdendritic region as well. On the other hand, V, Nb, and Cr are more localized in the interdendritic region. Point EDS of dendritic regions (DR), interdendritic regions (IDR), and the calculated melting temperature using the rule of a mixture of each region are listed in Table 5.

The melting temperature of DR is always higher than IDR since the former, W-rich, host elements with higher melting temperatures; this region is set to solidify first from the molten state and then followed by the solidification of IDR that has a lower melting temperature, the V-

rich, and lastly the laves phase with lowest melting temperature thus it is localized in the IDR. Mo and W have good chemical affinity and very close atomic radii; thus, they form a substitutional solid solution and form most of the DR; therefore, they are depleted in the interdendritic region. For the same reason, V and Cr are concentrated in the interdendritic region with their similar atomic radii and relatively low and close melting temperatures. From Miedema's table, the binary enthalpy of mixing shows that Nb-V is more positive than Nb-W and Nb-Mo; therefore, Nb is present mainly in the interdendritic region. On average, when considering a large enough region, the composition of the baseline alloy, WMoNbV, is close to nominal, with a small deviation from the starting blends. Cr amount is less than the nominal starting blends in all alloys. This could have been due to the scattering that takes place at the beginning of each melt and subsequent evaporation due to its higher vapor pressure during arc melting.

Based on SEM images, Image-J software was used to estimate the DR

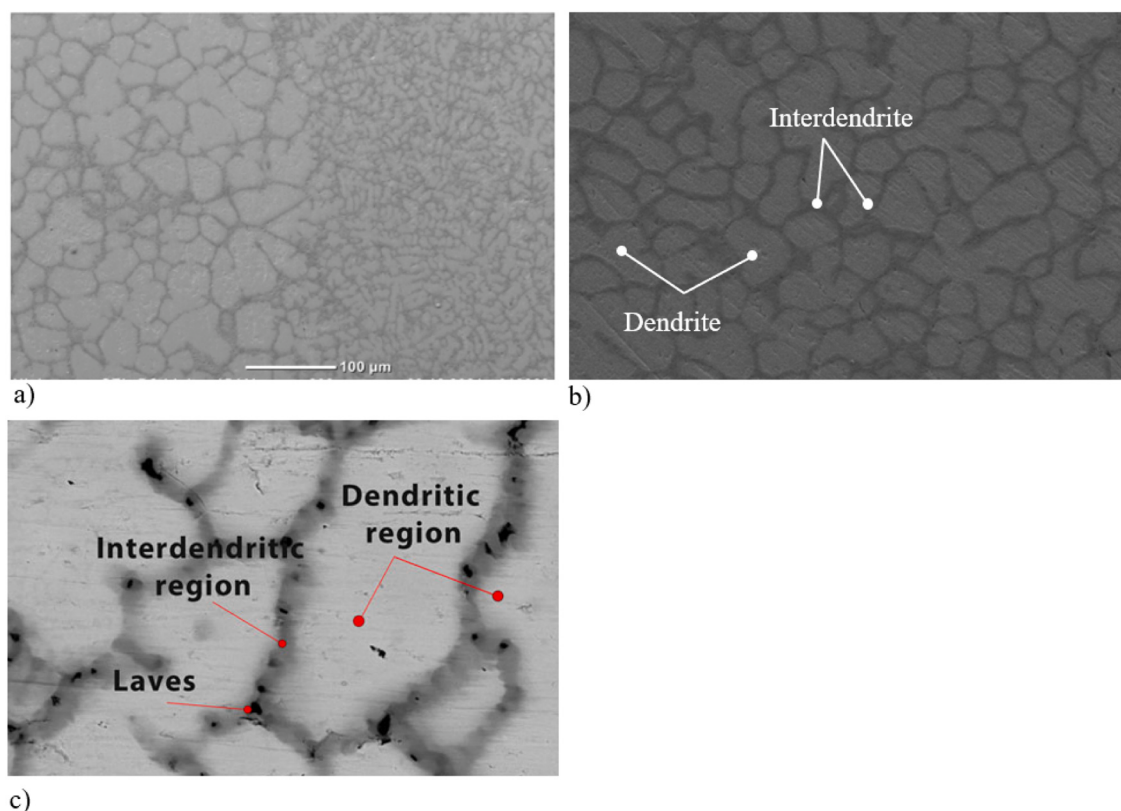


Fig. 4. SEM images showing (a) finer grains closer to the surface of the alloy in comparison to the center where a coarser microstructure. WMoNbVCr dendritic and interdendritic regions are shown in (b). BSE image of the same alloy shows laves phase localized in the IDR and presented in (c).

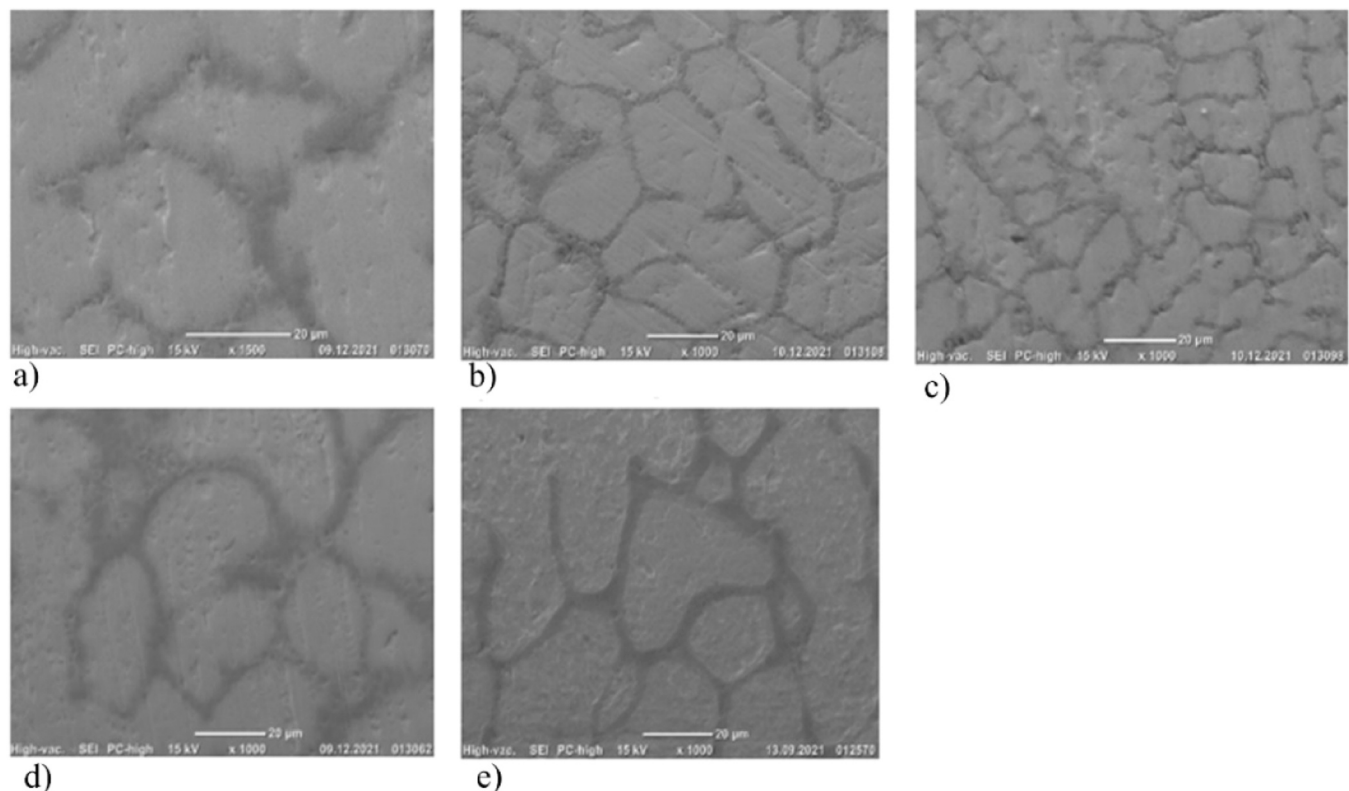


Fig. 5. SEM images of WMoNbVCr_x a) NO Cr b) Cr0.25c) Cr0.5 d) Cr0.75 and e) Cr1.

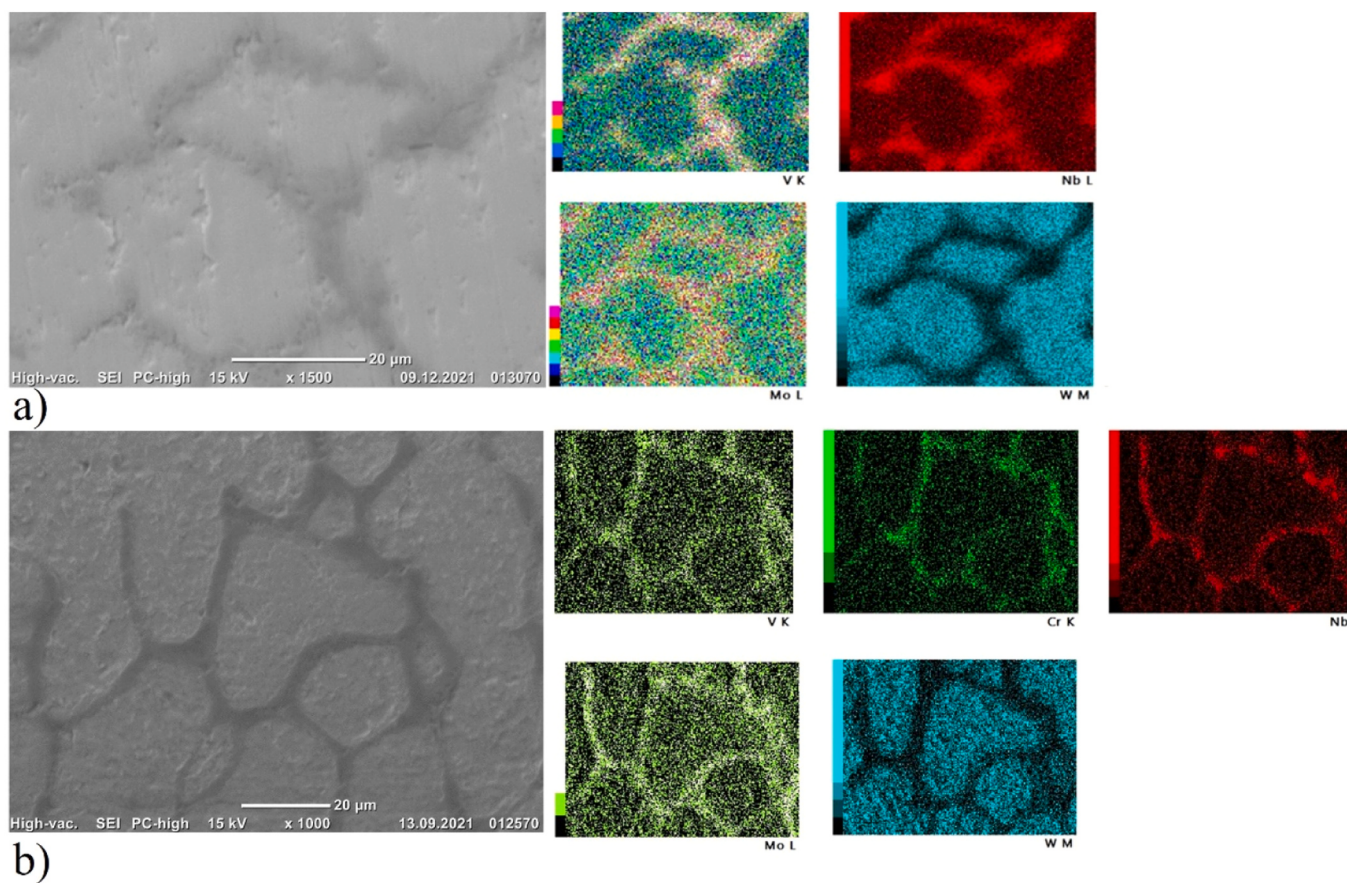


Fig. 6. SEM mapping analysis of (a) WMoNbV and (b) WMoNbVCr alloys. Localization of W is seen in the DR, whereas Nb, Cr, and V are more localized at IDR. Mo was relatively more evenly distributed.

Table 5

Chemical compositions obtained from point EDS of DR and IDR, general region EDS, melting temperature T_m , and volume fractions calculated using ImageJ software.

Alloy	Area	W (at. %)	Mo (at. %)	Nb (at. %)	V (at. %)	Cr (at. %)	T_m (°C)	ImageJ		DFT Calculations	
								Volume Fraction	Hv	Density per Region (g/cm ³)	a (Å) per region
WMoNbV	DR	38	26	21	16	0	2773.3	81 %	6.78	12.53	3.171
	IDR	9.9	21	33	36	0	2393.1	19 %	2.66	9.2	3.156
	Laves	1.7	3.3	22.3	72.7	0	2071.1	<1 %			
	Region	26.6	23.8	26.5	23.1	0					
WMoNbVCr _{0.25}	DR	34	29	21	14	2	2742.6	87 %	7.56	12.2	3.171
	IDR	12	16	31	38	3.1	2367.9	13 %	2.33	9.43	3.145
	Laves	4.3	3	21.5	70.2	1	2103.7	<1 %			
	Region	22.4	21.3	26.3	27.1	2.91					
WMoNbVCr _{0.5}	DR	38	24	21	12	4.6	2774.1	88 %	8.66	12.69	3.165
	IDR	10	20	28	37	5.1	2350.8	12 %	2.16	9.11	3.134
	Laves	0.6	3	23.9	70.3	2.2	2060.7	<1 %			
	Region	22.4	22.1	25.3	23.6	6.65					
WMoNbVCr _{0.75}	DR	46	22	18	11	3.4	2861	71 %	8.96	12.79	3.167
	IDR	2.3	35	35	20	7.8	2387.2	29 %	2.41	8.36	3.147
	Laves	1.2	0.8	25.6	70.6	1.8	2063.9	<1 %			
	Region	20.7	24.1	29.8	16.8	8.93					
WMoNbVCr	DR	44	24	16	12	3.8	2836	69 %	10.18	13.37	3.168
	IDR	6.6	14	28	31	20.5	2248.2	31 %	1.66	8.8	3.095
	Laves	1.3	1	13.9	74.6	9.1	1993.9	<1 %			
	Region	23.1	21.7	24	21.8	9.4					

and IDR volume fractions in each alloy. These volume fractions were the basis for estimating the lattice parameters and densities in DFT calculations. The density of each region was calculated separately, and based on the volume fraction of each region, the total density was calculated. Also, DFT calculations have been used to estimate the variations in the mechanical properties of each alloy based on the stoichiometry of the

DR and IDR chemical compositions obtained from point EDS and denoted as (Comp.). Considering these compositional changes and the volume fraction of each region, the computationally expected properties were generated and compared to the experimental data. It was found that the stoichiometry has a substantial impact on the mechanical properties of this alloy system. For a complete list of the computationally

predicted properties, refer to the [Supplementary Table S1](#).

[Fig. 7](#) shows the experimental lattice parameter and density versus the predicted DFT calculations. Experimental lattice parameters were calculated by taking the average lattice constant of 4 diffraction peaks of the BCC phase. [Fig. 7\(a\)](#) shows that both DFT nominal-based (nom.) and compositional-based (comp.) calculations follow the same downward trend, decreasing in lattice parameters and aligning with experimentally obtained values. [Fig. 7\(b\)](#) shows the density trends compared to experimental ones. It was found that the nominal density DFT trend aligns with the measured densities. The deviation in values from the measured ones indicates that the calculations didn't consider the porosities and the formation of minor Laves phase.

3.3. Mechanical properties

3.3.1. Microhardness

Vicker's microhardness measurements were carried out in the middle portion of the sample, which comprises a relatively larger dendritic structure, and at the edge of the sample with the finer dendritic structures. It was found that this central region shows a lower hardness than the edge of the sample that hosts a dense finer dendritic structure that is rich in W. We found that the alloy composition determines the hardness difference between the peripheries and the center, with Cr1 showing the maximum difference of 32.9 % in the measured values, as illustrated in [Fig. 8\(a\)](#). Thus, for consistency purposes, the reported microhardness values were measured in the middle portion of the sample. No cracks were initiated at the corners of the indentation, which signals ductile behavior as shown in [Fig. 8](#). This is explained by the DFT calculated Pugh's ratio values (bulk to shear modulus ratio), which are well above 1.7 (the critical value below which brittle behavior commences).

[Fig. 8 \(c\)](#) reveals the correlation between microhardness and chromium content. Microhardness increases with increasing Cr content, reaching a peak of 7.03 GPa at 0.5 mol Cr. Subsequently, it decreases, plateauing around 6.6–6.7 GPa for additions of 0.75 and 1.0 mol Cr to the base alloy. This trend mirrors the changes in the volume fraction of DR observed through microstructure analysis. Higher DR content coincides with increased hardness, suggesting the DR volume fraction plays a crucial role in the alloy's hardness.

DFT calculations support and explain these observations. The calculated hardness of DR consistently exceeds that of IDR due to its higher tungsten (W) content and lower vanadium (V) content. The DR hardness can be 3 times higher than that of the IDR, depending on the local variations in their stoichiometry. This explains the observed correlation between the DR volume fraction and overall hardness. Furthermore, [Fig. 8 \(c\)](#) demonstrates excellent agreement between the trend in calculated total hardness from DFT and the experimental data. This validates the DFT approach for understanding how compositional

changes induced by Cr addition affect microhardness and underscores the importance of studying non-equimolar compositions. Although it is the matching trend of DFT versus experimental hardness that is of utmost interest, from a quantitative perspective, the overestimation in the hardness values of DFT in comparison to the experimental data is in part attributed to the use of Vicker's microhardness during characterization, which had also been observed in the past [53]. An additional contributing factor is not considering the impact of dislocations and point defects in our DFT modeling here. Despite these limitations, the DFT calculated values capture the experimental trends perfectly, signifying the importance of local compositional changes in the mechanical behavior of the RHEA alloys synthesized.

3.3.2. Nanoindentation test

Nanoindentation testing has emerged as a pivotal technique in the study of wear behavior, offering invaluable insights into material response under abrasive conditions [35]. By precisely quantifying mechanical properties such as hardness and elastic modulus at nanoscales, nanoindentation assesses a material's resistance to deformation and penetration, which are fundamental factors in abrasive wear resistance. [56]. The load-displacement curves presented in [Fig. 9\(a\)](#) provide insight into the indentation behavior of various Cr-containing alloys, with an average of 10 indentation displacements reported. Notably, among these alloys, the 0.25Cr alloy exhibits the highest displacement, while the 0.5Cr alloy shows the lowest displacement. This discrepancy in displacement suggests differences in the mechanical response of these alloys to the applied load.

In [Fig. 9\(b\)](#), the theoretical elastic modulus, determined via DFT, is juxtaposed with the experimental elastic modulus obtained from the test. Theoretical elastic moduli were calculated based on the volume fraction of ID and IDR of each alloy. Both sets of elastic moduli exhibit a consistent trend, indicating a concurrence between computational predictions and experimental observations. This alignment lends credibility to both computational modeling and experimental methodologies for determining material properties.

Furthermore, the alloy with the lowest displacement in the load-displacement curves, namely the 0.5Cr sample, achieves the highest Young's modulus. This finding underscores the inverse relationship between displacement and elastic modulus: lower displacement correlates with higher elastic modulus, indicative of greater resistance to plastic deformation. The elastic modulus of DR is found to always be higher than that of IDR, and increasing Cr content consistently induces a higher Young's modulus in the dendritic structure.

3.3.3. Wear and friction test

[Fig. 10](#) shows the change in hardness with wear volume loss and the relationship with volume fractions of DR and IDR. The wear volume loss

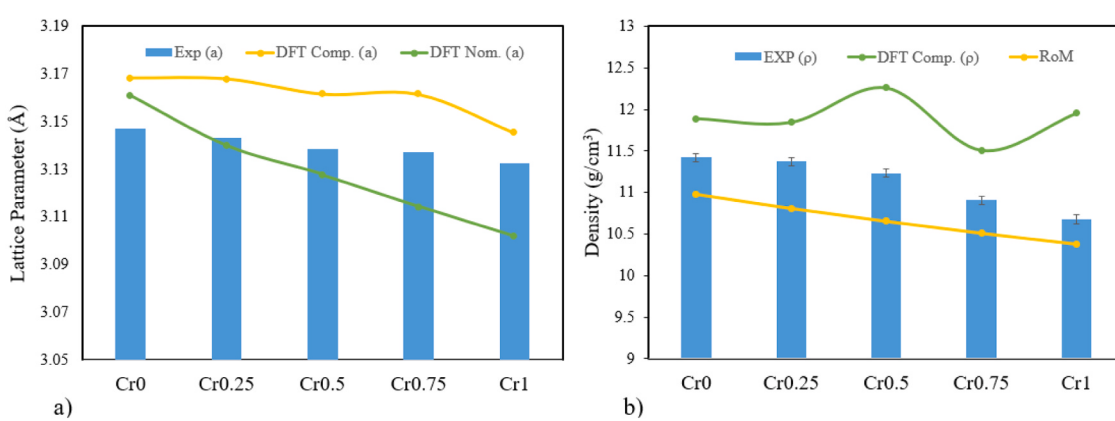


[Fig. 7](#). Calculated (a) lattice parameter and (b) density trends versus experimentally measured values are shown. Reduction in lattice parameter and density is an inevitable consequence of Cr addition due to smaller atomic radius.

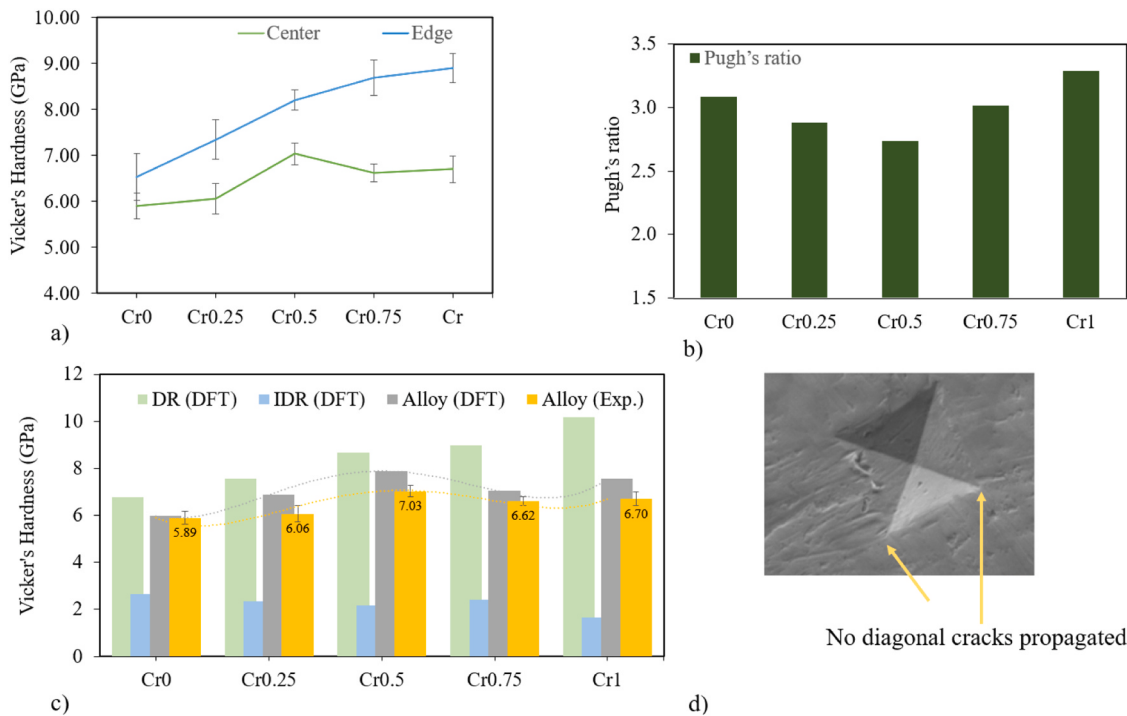


Fig. 8. a) Hardness at the center of the ingots compared to the edges. The central region shows a reduction in hardness b) DFT calculated Pugh's ratio shows highest ductile behavior in Cr0.5 Alloy c) DFT calculated hardness of dendritic (DR DFT), interdendritic (IDR DFT), the DR/IDR volume fraction-based hardness (Alloy DFT) and the experimental Vicker's microhardness. and d) The Indentation on the WMoNbVCr surface, demonstrating a ductile behavior as no fracture propagation was observed at the indentation diagonals.

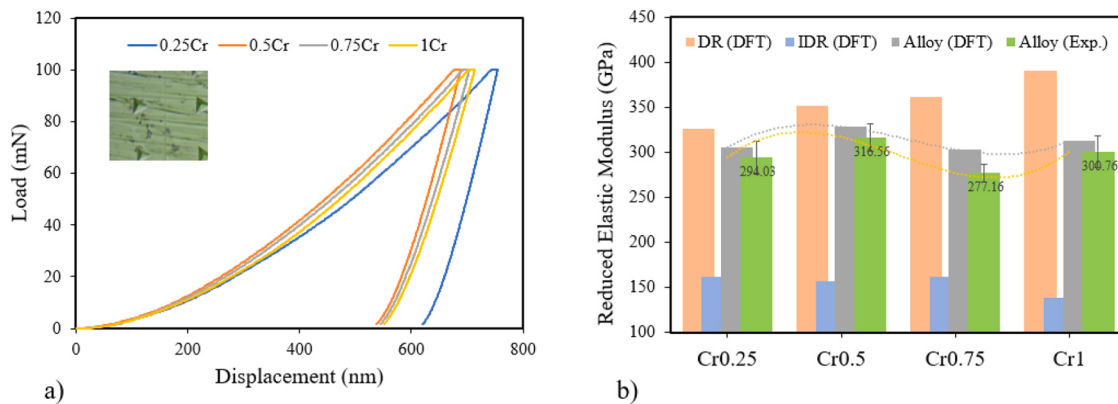


Fig. 9. nanoindentation test results a) load-displacement curves b) theoretical and experimental elastic moduli.

changed in perfect accordance with hardness in the inverse relationship. The volume fraction of DR increased with the increase in Cr addition, and a reduction in wear loss was observed.

The IDR volume fraction fluctuated proportionally with wear volume loss, which suggests the majority of the loss was from IDR which does not come as a surprise when considering the low hardness of IDR based on DFT calculations. However, after adding only 0.25 moles of Cr, there was a more than 58 % drop in volume loss, which is the highest compared with the other produced Cr_x alloys, where the change was within a range of 20 %–47 %. This drop resulted from solid solution strengthening due to lattice distortion caused by Cr addition, which subsequently coincided with an increase in the hardness of the DR regions. In other words, the alloy hardness and wear loss depend not only on the Cr content but also on the changes in hardness of the alloy's constituents, which are the DR and IDR, as well as their volume fractions. Prior literature [25,57] has attributed enhanced hardness to the effect of precipitation hardening caused by the minor Laves phase,

however, our study demonstrates the significant impact of Cr-induced changes in the hardness and fraction of DR and IDR as a major contributor as well. This experimental observation also directly supports the DFT-calculated changes in mechanical properties as a function of stoichiometry.

The lowest volume loss in as-cast ingots was achieved after adding 0.5 moles of Cr, however, wear properties generally improved after adding Cr to the base alloy.

The surface chemistry analysis of the Cr containing alloys by XPS shows the formation of tribo-oxides, and Cr₂O₃ (Fig. 11 a), which is a well-known compact passive layer that protects the alloy by increasing surface hardness and reducing further oxidation kinetics of the alloy. Wear tracks shown in Fig. 11 (b) and (c) demonstrate the apparent effect of Cr addition on the coefficient of friction and wear volume loss when comparing Cr0 vs. Cr1 alloys. Wear track was more obvious in the Cr0 alloy, and adhesive wear was obviously visible. To systematically study the wear resistance of WMoNbVCr_x alloys with higher hardness, the

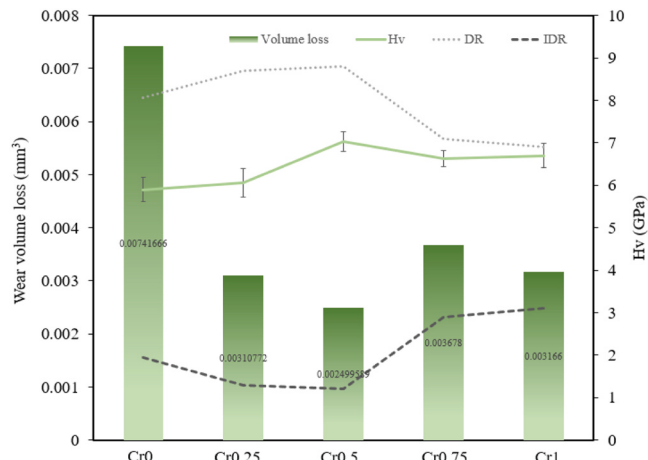


Fig. 10. Wear volume loss reduces with Cr addition to the base alloy, and a generally increasing hardness trend is observed. However, it is the dendritic volume (DR) that closely follows the hardness trend, signifying the importance of volume fractions of each DR and IDR in the final wear resistance of the synthesized alloys.

effect of increasing Cr content on the wear resistance of WMoNbVCr_x RHEAs was investigated. In the realm of high entropy alloys, the degree of fluctuation in the wear coefficient curves is intricately tied to both the phase composition of the alloy's microstructure and the uniformity of that microstructure within the alloy [58]

Fig. 12 (a) illustrates the friction coefficient curve variation graph of WMoNbVCr_x with different Cr additions in correspondence with distance. Wear profiles are shown in **Fig. 12** (b) with different Cr content. After adding 0.5 moles of Cr to the base alloy, the wear profiles decrease significantly, and the fluctuation in coefficient of friction curves is reduced to be steadier in Cr0.5, Cr0.75, and Cr1 alloys. Alphan et. al. [35] has already demonstrated the importance of passive oxide film formation on RHEAs for reduction in the coefficient of friction and improved wear resistance. We observe the same effects here due to formation of the tribo-oxides. At the commencement of dry sliding

friction, a momentary and distinct rise is observed in the alloy's friction coefficient, especially when the amount of Cr is <0.5 mole attributed to greater material pile-up due to lower hardness values, as explained by Trzepieciński and Lemu [59] and progressive rise in contact friction as the alloy's sliding cycles accumulate. This is followed by a stabilization phase, marked by reduced fluctuations, as the alloy undergoes friction. This behavior can be attributed to the progressive rise in contact friction as the alloy's sliding cycles accumulate. The alloy surface undergoes wear due to fatigue-induced damage, concurrently generating particle fragments on its surface that contribute to abrasive wear as an additional wear mechanism. This was more evident in Cr0.25 and Cr0 alloys. Notably, the alloy's capability to create a third body between opposing sides might have contributed to its heightened friction coefficient [60]. The alloys display minimum fluctuations in their friction curves after a 10 m distance specially when Cr content was \geq 0.5 moles. The average friction coefficients for the five RHEAs ranged from 0.35 in Cr0.5 to 0.55 in Cr0. Interestingly, the friction coefficient exhibits a decreasing trend with increasing Cr content, this could be due to lower material pile-up because of the hard oxide layer and the increased hardness of the alloy. Consistent with the friction coefficient trend, wear loss decreases with increasing Cr content. However, the alloys Cr0.75 and Cr1 exhibit a bit higher wear loss. This suggests that while chromium generally enhances wear resistance, there may be an optimal chromium content for maximum wear resistance. Notably, the alloy with 0.5 moles of Cr exhibits the lowest coefficient of friction and wear loss, as evidenced by its smooth wear curve. This is explained by the fact that Cr0.5 exhibits the highest hardness and Young's modulus, which consequently results in superior wear resistance. This highlights the superior wear resistance of chromium-containing RHEAs, making them particularly suitable for wear applications.

4. Conclusions

In this study WMoNbVCr_x ($x = 0, 0.25, 0.5, 0.75$ and 1) refractory high entropy alloys have been designed using the CALPHAD method and DFT to predict alloy properties. The alloys have been experimentally produced using vacuum arc melting. The primary conclusions are:

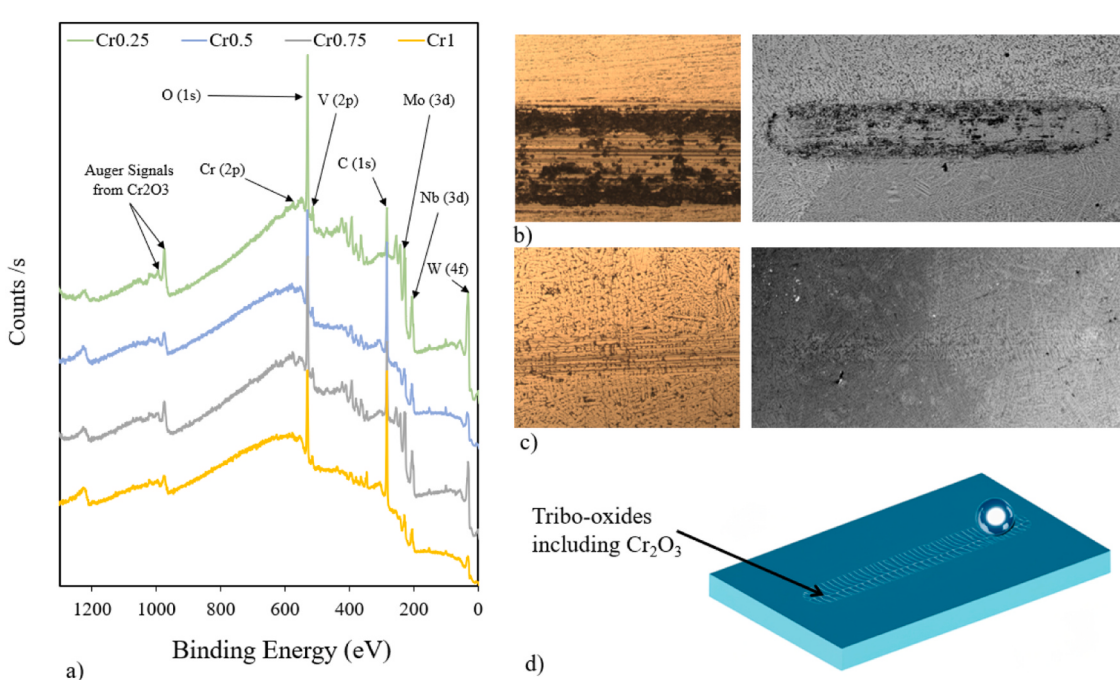


Fig. 11. (a) XPS analysis of the surface showing tribo-oxide formation, (b) Optical and SEM images of wear track of alloys containing no Cr addition, Cr0, and with 1 mol of Cr, Cr1 (c), shows the addition of Cr significantly enhances the wear resistance. (d) schematic illustration of wear track.

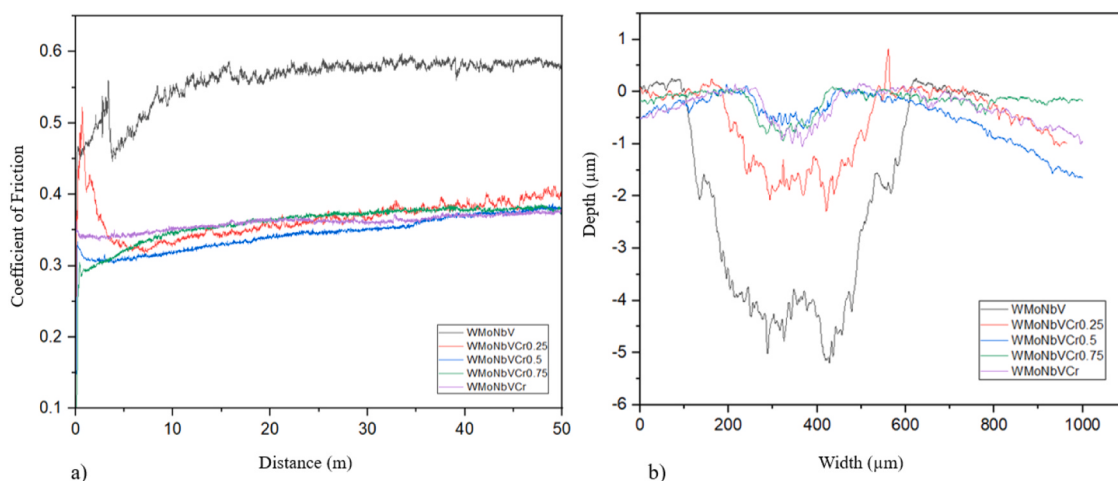


Fig. 12. The coefficient of friction (a) and wear profiles (b) for alloys containing different Cr contents are shown. With increasing Cr content, a reduction in the coefficient of friction and a smoothening of the wear profiles are observed, which can be attributed to enhanced wear properties.

- A single-phase BCC structure is computationally predicted with stoichiometric variations. These changes in stoichiometries influenced the mechanical properties.
- The trends in the properties of computationally designed alloys and experimentally prepared alloys matched, proving that the computational models and consolidation methods matched.
- DFT calculations revealed that the dendritic region consistently exhibited the highest hardness and Young's modulus, whereas the interdendritic region consistently displayed the lowest hardness across all alloys.
- The DFT calculations demonstrate that non-equimolar stoichiometries of the dendrites rich in W are significantly harder (~ 10 GPa), while the interdendritic stoichiometries rich in V are softer (~ 2 GPa).
- Solid solution strengthening was the major contributor to improved mechanical properties, which was apparent after adding 0.25 moles of Cr to the base alloy.
- The base alloy WMoNbV had the lowest Vicker's microhardness of 5.89 GPa with the highest wear volume loss of 7.32×10^{-3} mm³.
- Nanoindentation Young's modulus followed the same trend as in DFT calculations, with the highest elastic modulus of 316.56 GPa for the WMoNbVCr_{0.5} alloy.
- Adding Cr to the base alloy increased microhardness to reach the highest microhardness in WMoNbVCr_{0.5} with $7.03 \text{ GPa} \pm 0.24$ and the lowest wear volume loss of 2.5×10^{-3} mm³.
- The coefficient of friction fluctuation significantly dropped as the content of Cr exceeded 0.5 mols, which concluded that less abrasive wear was taking place as there were not three surface particles between the two surfaces. This could make the alloy more reliable for applications where consistent load performance is essential.
- This study also demonstrates the effectiveness of computational alloy design through CALPHAD and DFT based on molar stoichiometries for novel materials design as the experimental trends were perfectly captured by the first principles calculations.

CRediT authorship contribution statement

Faruk Kaya: Data curation. **Hasan Gökçe:** Formal analysis. **Burçak Boztemur:** Writing – review & editing, Conceptualization. **Mubashir Mansoor:** Writing – review & editing, Writing – original draft, Visualization, Software, Methodology, Formal analysis, Conceptualization. **Ammar Basil Nader Alkraidi:** Writing – review & editing, Writing – original draft, Visualization, Validation, Software, Resources, Methodology, Investigation, Funding acquisition, Formal analysis, Data curation, Conceptualization. **M. Lütfi Öveçoglu:** Writing – review & editing,

Supervision, Project administration, Funding acquisition. **Duygu Ağaogulları:** Writing – review & editing, Project administration. **Bora Derin:** Formal analysis, Conceptualization. **Cennet Yıldırım:** Data curation.

Declaration of Competing Interest

The authors declare that they have no known competing financial interests or personal relationships that could have appeared to influence the work reported in this paper.

Data availability

Data will be made available on request.

Acknowledgements

This project is supported by TUBITAK with project number 119M980. Thanks to Assoc. Prof. Dr. Bedri Baksan for their help and support in vacuum arc melting. We also appreciate the support of Assoc. Prof. Dr. Zuhal Er, thank you for facilitating access to the UHeM supercomputer through project number 1008852020. Thanks to research assistant Mertcan Kaba for his help and support on wear test.

Appendix A. Supporting information

Supplementary data associated with this article can be found in the online version at [doi:10.1016/j.jallcom.2024.175510](https://doi.org/10.1016/j.jallcom.2024.175510).

References

- [1] J.-W. Yeh, S.-K. Chen, S.-J. Lin, J.-Y. Gan, T.-S. Chin, T.-T. Shun, C.-H. Tsau, S.-Y. Chang, Nanostructured high-entropy alloys with multiple principal elements: novel alloy design concepts and outcomes, *Adv. Eng. Mater.* 6 (2004) 299–303, <https://doi.org/10.1002/adem.200300567>.
- [2] Y. Zhang, Y.J. Zhou, J.P. Lin, G.L. Chen, P.K. Liaw, Solid-solution phase formation rules for multi-component alloys, *Adv. Eng. Mater.* 10 (2008) 534–538, <https://doi.org/10.1002/adem.200700240>.
- [3] X. Yang, Y. Zhang, Prediction of high-entropy stabilized solid-solution in multi-component alloys, *Mater. Chem. Phys.* 132 (2012) 233–238, <https://doi.org/10.1016/j.matchemphys.2011.11.021>.
- [4] Z. Wang, Y. Huang, Y. Yang, J. Wang, C.T. Liu, Atomic-size effect and solid solubility of multicomponent alloys, *Scr. Mater.* 94 (2015) 28–31, <https://doi.org/10.1016/j.scriptamat.2014.09.010>.
- [5] O.N. Senkov, G.B. Wilks, D.B. Miracle, C.P. Chuang, P.K. Liaw, Refractory high-entropy alloys, *Intermet.* (Barking) 18 (2010) 1758–1765, <https://doi.org/10.1016/j.intermet.2010.05.014>.

- [6] Y. Zhang, T.T. Zuo, Z. Tang, M.C. Gao, K.A. Dahmen, P.K. Liaw, Z.P. Lu, Microstructures and properties of high-entropy alloys, *Prog. Mater. Sci.* 61 (2014) 1–93, <https://doi.org/10.1016/j.pmatsci.2013.10.001>.
- [7] S.G. Ma, Z.M. Jiao, J.W. Qiao, H.J. Yang, Y. Zhang, Z.H. Wang, Strain rate effects on the dynamic mechanical properties of the AlCrCuFeNi2 high-entropy alloy, *Mater. Sci. Eng. A* 649 (2016) 35–38, <https://doi.org/10.1016/j.msea.2015.09.089>.
- [8] K. Hua, Q. Wan, Z. Zhou, Q. Zhou, X. Li, H. Wu, H. Wang, Enhanced wear-resistance of TiZrHfNb refractory high entropy alloys mediated by subsurface instabilities, *Mater. Lett.* 311 (2022), <https://doi.org/10.1016/j.matlet.2021.131612>.
- [9] C.-Y. Hsu, J.-W. Yeh, S.-K. Chen, T.-T. Shun, Wear resistance and high-temperature compression strength of Fcc CuCoNiCrAl0.5Fe alloy with boron addition, *Metall. Mater. Trans. A* 35 (2004) 1465–1469, <https://doi.org/10.1007/s11661-004-0254-x>.
- [10] B. Chen, X. Li, W. Chen, L. Shang, L. Jia, Microstructural evolution, mechanical and wear properties, and corrosion resistance of as-cast CrFeNbTiMox Refractory high entropy alloys, *Intermetallics* 155 (2023) 107829, <https://doi.org/10.1016/j.intermet.2023.107829>.
- [11] O.N. Senkov, G.B. Wilks, J.M. Scott, D.B. Miracle, Mechanical properties of Nb₂₅Mo₂₅Ta₂₅W₂₅ and V₂₀Nb₂₀Mo₂₀Ta₂₀W₂₀ refractory high entropy alloys, *Intermetallics* 19 (2011) 698–706, <https://doi.org/10.1016/j.intermet.2011.01.004>.
- [12] A.D. Akinwekomi, F. Akhtar, Bibliometric mapping of literature on high-entropy/multicomponent alloys and systematic review of emerging applications, *Entropy* 24 (2022) 329, <https://doi.org/10.3390/e24030329>.
- [13] M. Zhang, L.G. Hector, Y. Guo, M. Liu, L. Qi, First-principles search for alloying elements that increase corrosion resistance of Mg with second-phase particles of transition metal impurities, *Comput. Mater. Sci.* 165 (2019) 154–166, <https://doi.org/10.1016/j.commatsci.2019.04.018>.
- [14] M. Wu, S. Wang, H. Huang, D. Shu, B. Sun, CALPHAD aided eutectic high-entropy alloy design, *Mater. Lett.* 262 (2020) 127175, <https://doi.org/10.1016/j.matlet.2019.127175>.
- [15] J. Zhang, C. Cai, G. Kim, Y. Wang, W. Chen, Composition design of high-entropy alloys with deep sets learning, *NPJ Comput. Mater.* 8 (2022) 89, <https://doi.org/10.1038/s41524-022-00779-7>.
- [16] O.N. Senkov, D.B. Miracle, K.J. Chaput, J.P. Couzinie, Development and exploration of refractory high entropy alloys - A review, *J. Mater. Res.* 33 (2018) 3092–3128, <https://doi.org/10.1557/jmr.2018.153>.
- [17] Y. Ikeda, B. Grabowski, F. Körmann, Ab initio phase stabilities and mechanical properties of multicomponent alloys: a comprehensive review for high entropy alloys and compositionally complex alloys, *Mater. Charact.* 147 (2019) 464–511, <https://doi.org/10.1016/j.matchar.2018.06.019>.
- [18] M.C. Gao, C.S. Carney, Ö.N. Doğan, P.D. Jablonksi, J.A. Hawk, D.E. Alman, Design of REfractory High-entropy Alloys, *JOM* 67 (2015) 2653–2669, <https://doi.org/10.1007/s11837-015-1617-z>.
- [19] S.M. Shaikh, V.S. Hariharan, S.K. Yadav, B.S. Murty, CALPHAD and rule-of-mixtures: a comparative study for refractory high entropy alloys, *Intermetallics* 127 (2020) 106926, <https://doi.org/10.1016/j.intermet.2020.106926>.
- [20] M. Vaghari, K. Dehghani, Computational and experimental investigation of a new non-equiaxed FCC single-phase Cr₁₅Cu₅Fe₂₀Mn₂₅Ni₃₅ high-entropy alloy, *Phys. B Condens Matter* 671 (2023) 415413, <https://doi.org/10.1016/j.physb.2023.415413>.
- [21] P. Sarker, T. Harrington, C. Toher, C. Oses, M. Samiee, J.-P. Maria, D.W. Brenner, K.S. Vecchio, S. Curtarolo, High-entropy high-hardness metal carbides discovered by entropy descriptors, *Nat. Commun.* 9 (2018) 4980, <https://doi.org/10.1038/s41467-018-07160-7>.
- [22] H.H. Kristoffersen, J. Rossmeisl, Local order in AgAuCuPdPt high-entropy alloy surfaces, *J. Phys. Chem. C* 126 (2022) 6782–6790, <https://doi.org/10.1021/acs.jpcc.2c00478>.
- [23] T. Li, O.J. Swanson, G.S. Frankel, A.Y. Gerard, P. Lu, J.E. Saal, J.R. Scully, Localized corrosion behavior of a single-phase non-equimolar high entropy alloy, *Electro Acta* 306 (2019) 71–84, <https://doi.org/10.1016/j.electacta.2019.03.104>.
- [24] Z. Wang, S. Chen, S. Yang, Q. Luo, Y. Jin, W. Xie, L. Zhang, Q. Li, Light-weight refractory high-entropy alloys: a comprehensive review, *J. Mater. Sci. Technol.* 151 (2023) 41–65, <https://doi.org/10.1016/j.jmst.2022.11.054>.
- [25] L. Fang, J. Wang, X. Li, X. Tao, Y. Ouyang, Y. Du, Effect of Cr content on microstructure characteristics and mechanical properties of ZrNbTaHf_{0.2}Cr_x refractory high entropy alloy, *J. Alloy. Compd.* 924 (2022) 166593, <https://doi.org/10.1016/j.jallcom.2022.166593>.
- [26] J. Yan, M. Li, K. Li, J. Qiu, Y. Guo, Effects of Cr Content on Microstructure and Mechanical Properties of WMoNbTiCr High-Entropy Alloys, *J. Mater. Eng. Perform.* 29 (2020) 2125–2133, <https://doi.org/10.1007/s11665-020-04744-7>.
- [27] N.D. Stepanov, N.Y. Yurchenko, D.V. Skibin, M.A. Tikhonovsky, G.A. Salishchev, Structure and mechanical properties of the AlCr_xNbTiV (x = 0, 0.5, 1, 1.5) high entropy alloys, *J. Alloy. Compd.* 652 (2015) 266–280, <https://doi.org/10.1016/j.jallcom.2015.08.224>.
- [28] N. Yurchenko, E. Panina, S. Zherebtsov, N. Stepanov, Design and characterization of eutectic refractory high entropy alloys, *Mater. (Oxf.)* 16 (2021) 101057, <https://doi.org/10.1016/j.mtla.2021.101057>.
- [29] C. Mathiou, A. Poulia, E. Georgatis, A.E. Karantzas, Microstructural features and dry - Sliding wear response of MoTaNbZrTi high entropy alloy, *Mater. Chem. Phys.* 210 (2018) 126–135, <https://doi.org/10.1016/j.matchemphys.2017.08.036>.
- [30] M. Pole, M. Sadeghilaridjani, J. Shittu, A. Ayyagari, S. Mukherjee, High temperature wear behavior of refractory high entropy alloys based on 4-5-6 elemental palette, *J. Alloy. Compd.* 843 (2020) 156004, <https://doi.org/10.1016/j.jallcom.2020.156004>.
- [31] X. Pei, Y. Du, X. Hao, H. Wang, Q. Zhou, H. Wu, H. Wang, Microstructure and tribological properties of TiZrV0.5Nb0.5Al refractory high entropy alloys at elevated temperature, *Wear* 488–489 (2022) 204166, <https://doi.org/10.1016/j.wear.2021.204166>.
- [32] A. Poulia, E. Georgatis, A. Karantzas, Evaluation of the microstructural aspects, mechanical properties and dry sliding wear response of MoTaNbV₂Ti refractory high entropy alloy, *Met. Mater. Int.* 25 (2019) 1529–1540, <https://doi.org/10.1007/s12540-019-00283-6>.
- [33] A. Poulia, E. Georgatis, A. Lekatou, A.E. Karantzas, Microstructure and wear behavior of a refractory high entropy alloy, *Int. J. Refract. Met. Hard Mater.* 57 (2016) 50–63, <https://doi.org/10.1016/j.ijrmhm.2016.02.006>.
- [34] V. Bhardwaj, Q. Zhou, F. Zhang, W. Han, Y. Du, K. Hua, H. Wang, Effect of Al addition on the microstructure, mechanical and wear properties of TiZrNbHf₂ refractory high entropy alloys, *Tribol. Int.* 160 (2021) 107031, <https://doi.org/10.1016/j.triboint.2021.107031>.
- [35] Y. Alphan, M. Kaba, A. Motallebzadeh, H. Cimenoglu, Oxidation of a refractory high entropy alloy (RHEA) at moderate temperatures for wear related applications, *Int. J. Refract. Met. Hard Mater.* 113 (2023) 106223, <https://doi.org/10.1016/j.ijrmhm.2023.106223>.
- [36] Z. Li, Y. Jiang, R. Zhou, Z. Chen, Q. Shan, J. Tan, Effect of Cr addition on the microstructure and abrasive wear resistance of WC-reinforced iron matrix surface composites, *J. Mater. Res.* 29 (2014) 778–785, <https://doi.org/10.1557/jmr.2014.38>.
- [37] J. Ju, H.-G. Fu, D.-M. Fu, S.-Z. Wei, P. Sang, Z.-W. Wu, K.-Z. Tang, Y.-P. Lei, Effects of Cr and V additions on the microstructure and properties of high-vanadium wear-resistant alloy steel, *Ironmak. Steelmak.* 45 (2018) 176–186, <https://doi.org/10.1080/03019233.2016.1250491>.
- [38] Y. Tian, J. Ju, H. Fu, S. Ma, J. Lin, Y. Lei, Effect of chromium content on microstructure, hardness, and wear resistance of As-Cast Fe-Cr-B alloy, *J. Mater. Eng. Perform.* 28 (2019) 6428–6437, <https://doi.org/10.1007/s11665-019-04369-5>.
- [39] S. Waqar, A. Wadood, A. Mateen, M.A.U. Rehman, Effects of Ni and Cr addition on the wear performance of NiTi alloy, *Int. J. Adv. Manuf. Technol.* 108 (2020) 625–634, <https://doi.org/10.1007/s00170-020-05380-0>.
- [40] M. Zhang, L. Zhang, J. Fan, P. Yu, G. Li, Anomalous microstructure and excellent mechanical behaviors of (CoCrFeNi) Cr Al high-entropy alloy induced by Cr and Al addition, *Mater. Sci. Eng. A* 752 (2019) 63–74, <https://doi.org/10.1016/j.msea.2019.02.071>.
- [41] B. Boztemur, K.G. Bayrak, H. Gökc, E. Ayas, Ö. Balci-Çağiran, B. Derin, D. Ağaogulları, M.L. Öveçoglu, Mechanically alloyed and spark plasma sintered WNbMoV₂Ta refractory high entropy alloys: effects of Cr and Al on the microstructural and mechanical properties, *J. Alloy. Compd.* 965 (2023) 171415, <https://doi.org/10.1016/j.jallcom.2023.171415>.
- [42] O.N. Senkov, J.M. Scott, S.V. Senkova, D.B. Miracle, C.F. Woodward, Microstructure and room temperature properties of a high-entropy TaNbHfZrTi alloy, *J. Alloy. Compd.* 509 (2011) 6043–6048, <https://doi.org/10.1016/j.jallcom.2011.02.171>.
- [43] J.P. Perdew, K. Burke, M. Ernzerhof, Generalized gradient approximation made simple, *Phys. Rev. Lett.* 77 (1996) 3865–3868, <https://doi.org/10.1103/PhysRevLett.77.3865>.
- [44] P.E. Blöchl, Projector augmented-wave method, *Phys. Rev. B* 50 (1994) 17953–17979, <https://doi.org/10.1103/PhysRevB.50.17953>.
- [45] Y. Le Page, P. Saxe, Symmetry-general least-squares extraction of elastic coefficients from *ab initio* total energy calculations, *Phys. Rev. B* 63 (2001) 174103, <https://doi.org/10.1103/PhysRevB.63.174103>.
- [46] Y. Le Page, P. Saxe, Symmetry-general least-squares extraction of elastic data for strained materials from *ab initio* calculations of stress, *Phys. Rev. B* 65 (2002) 104104, <https://doi.org/10.1103/PhysRevB.65.104104>.
- [47] D.H. Chung, W.R. Buessem, The Voigt-Reuss-Hill (VRH) approximation and the elastic moduli of polycrystalline ZnO, TiO₂ (Rutile), and α -Al₂O₃, *J. Appl. Phys.* 39 (1968) 2777–2782, <https://doi.org/10.1063/1.1656672>.
- [48] O.N. Senkov, D.B. Miracle, Generalization of intrinsic ductile-to-brittle criteria by Pugh and Pettifor for materials with a cubic crystal structure, *Sci. Rep.* 11 (2021) 4531, <https://doi.org/10.1038/s41598-021-83953-z>.
- [49] C. Örnek, M. Mansoor, A. Larsson, F. Zhang, G.S. Harlow, R. Kroll, F. Carlå, H. Hussain, B. Derin, U. Kivisäkk, D.L. Engelberg, E. Lundgren, J. Pan, The causation of hydrogen embrittlement of duplex stainless steel: phase instability of the austenite phase and ductile-to-brittle transition of the ferrite phase – Synergy between experiments and modelling, *Corros. Sci.* 217 (2023) 111140, <https://doi.org/10.1016/j.corsci.2023.111140>.
- [50] Y. Tian, B. Xu, Z. Zhao, Microscopic theory of hardness and design of novel superhard crystals, *Int. J. Refract. Met. Hard Mater.* 33 (2012) 93–106, <https://doi.org/10.1016/j.ijrmhm.2012.02.021>.
- [51] O.L. Anderson, A simplified method for calculating the debye temperature from elastic constants, *J. Phys. Chem. Solids* 24 (1963) 909–917, [https://doi.org/10.1016/0022-3697\(63\)90067-2](https://doi.org/10.1016/0022-3697(63)90067-2).
- [52] B. Boztemur, M. Mansoor, F. Kaya, M. Huang, E. Tekoğlu, M.L. Öveçoglu, J. Li, D. Ağaogulları, NbB₆ ceramic nanoparticles: first principles calculations, mechanochemical synthesis and strain engineering, *J. Mater. Res. Technol.* 24 (2023) 5571–5587, <https://doi.org/10.1016/j.jmrt.2023.04.165>.
- [53] S. Kavak, K.G. Bayrak, M. Mansoor, M. Kaba, E. Ayas, Ö. Balci-Çağiran, B. Derin, M.L. Öveçoglu, D. Aşaogulları, First principles calculations and synthesis of multi-phase (HTfIWzr)B₂ high entropy diboride ceramics: microstructural, mechanical

- and thermal characterization, *J. Eur. Ceram. Soc.* 43 (2023) 768–782, <https://doi.org/10.1016/j.jeurceramsoc.2022.10.047>.
- [54] H. Niu, S. Niu, A.R. Oganov, Simple and accurate model of fracture toughness of solids, *J. Appl. Phys.* 125 (2019), <https://doi.org/10.1063/1.5066311>.
- [55] P.A. Ferreira, S.O. von Tiedemann, N. Parkes, D. Gurah, D.J.M. King, P. Norman, M.R. Gilbert, A.J. Knowles, VNbCrMo refractory high-entropy alloy for nuclear applications, *Int J. Refract. Met. Hard Mater.* 113 (2023) 106200, <https://doi.org/10.1016/j.ijrmhm.2023.106200>.
- [56] R. Saha, W.D. Nix, Effects of the substrate on the determination of thin film mechanical properties by nanoindentation, *Acta Mater.* 50 (2002) 23–38, [https://doi.org/10.1016/S1359-6454\(01\)00328-7](https://doi.org/10.1016/S1359-6454(01)00328-7).
- [57] J. Yan, M. Li, K. Li, J. Qiu, Y. Guo, Effects of Cr content on microstructure and mechanical properties of WMoNbTiCr high-entropy alloys, *J. Mater. Eng. Perform.* 29 (2020) 2125–2133, <https://doi.org/10.1007/s11665-020-04744-7>.
- [58] Y. Guo, L. Liu, Y. Zhang, J. Qi, B. Wang, Z. Zhao, J. Shang, J. Xiang, A superfine eutectic microstructure and the mechanical properties of CoCrFeNiMo_x high-entropy alloys, *J. Mater. Res.* 33 (2018) 3258–3265, <https://doi.org/10.1557/jmr.2018.177>.
- [59] T. Trzepiecinski, H.G. Lemu, Numerical analysis of the influence of friction conditions on the pile-up effect in Vickers hardness measurements, *IOP Conf. Ser. Mater. Sci. Eng.* 700 (2019) 012019, <https://doi.org/10.1088/1757-899X/700/1/012019>.
- [60] C.-Y. Hsu, J.-W. Yeh, S.-K. Chen, T.-T. Shun, Wear resistance and high-temperature compression strength of Fcc CuCoNiCrAl0.5Fe alloy with boron addition, *Mater. Mater. Trans. A* 35 (2004) 1465–1469, <https://doi.org/10.1007/s11661-004-0254-x>.